Bayesian parameter estimation for space and time interacting earthquake rupture model using historical and physics-based simulated earthquake catalogs

Luis Ceferino[1], Percy Galvez[2,3], Jean-Paul Ampuero[4], Anne Kiremidjian[1], Gregory Deierlein[1], and Juan C. Villegas-Lanza[5]

[1]Civil and Environmental Engineering Department, Stanford University
[2]King Abdullah University of Science and Technology
[3]ETH Zurich
[4]Université Côte d'Azur, IRD, CNRS, Observatoire de la Côte d'Azur, Géoazur
[5]Instituto Geofísico del Perú
[1]450 Serra Mall, Stanford, CA 94305
[2]Thuwal 23955, Saudi Arabia
[3]Rämistrasse 101, 8092 Zurich, Switzerland
[4]250 Rue Albert Einstein, 06560 Valbonne, France
[5]Calle Badajoz N 169 Urb. Mayorazgo IV Etapa, Lima, Perú

November 26, 2020

Corresponding author: Luis Ceferino. E-mail: lceferinor@gmail.com
Preprint submitted to the Bulletin of the Seismological Society of America

Abstract

This paper introduces a framework to supplement short historical catalogs with synthetic catalogs and determine large earthquakes' recurrence. For this assessment, we developed a parameter estimation technique for a probabilistic earthquake occurrence model that captures time and space interactions between large mainshocks. The technique is based on a two-step Bayesian update that uses a synthetic catalog from physics-based simulations for initial parameter estimation and then the historical catalog for further parameter calibration. The paper also provides a formulation to combine multiple synthetic catalogs according to their likelihood of representing empirical earthquake stress drops and GPS-inferred interseismic coupling. We applied this technique to analyze large-magnitude earthquakes' recurrence along 650 km of the subduction fault's interface, located offshore Lima, Peru. We built nine 2,000-years-long synthetic catalogs using quasi-dynamic earthquake cycle simulations based on the rate-and-state friction law to supplement the 450-year-long historical catalog. The synthetic catalogs' validity was verified by comparing their annual magnitude exceedence rates to those of recorded seismicity. When the synthetic catalogs are combined with the historical catalog without considering their variability, we found average relative reductions larger than 90% in the recurrence parameters' uncertainty. When the uncertainty in the physics-based simulations is propagated to the posterior, the reductions in uncertainty decrease to 60%-70%. We then demonstrate that using synthetic catalogs results in higher reductions in parameter uncertainty than using only the historical catalog (69% vs. 60%), demonstrating that synthetic catalogs can effectively supplement short synthetic catalogs, especially in regions with little earthquake recurrence's apriori knowledge. Finally, we show the implications of these results for time-dependent seismic hazard.

INTRODUCTION

Recent earthquake observations and improvements in understanding the mechanics of earthquake rupture processes have enabled advanced probabilistic models for time-dependent earthquake hazards (Akinci et al., 2009; Field, 2015; Ceferino et al., 2020). Even though these probabilistic models can capture complex spatiotemporal interactions between earthquakes, they still face two main challenges.

First, these complex models lack suitable parameter estimation techniques based on either the frequentist approach using maximum likelihood estimation (MLE) or the Bayesian approach. Often-used simplified parameter estimation techniques can lead to unreliable parameter estimates for these complex models (Field, 2015; Ceferino et al., 2020).

Second, earthquake catalogs are too short compared to the long interevent times of large magnitude earthquakes, which introduces large uncertainties in the parameter estimates. Most complete earthquake catalogs cover periods from a few decades to several hundred years, depending on the region and earthquake magnitude of analysis. Because large earthquakes, e.g., Mw > 8.0, often have long return periods, historical catalogs are often insufficient to characterize large earthquakes' recurrence time, e.g., Parsons et al. (2012).

Thus, time-dependent seismic hazard analyses based on such complex earthquake models can have low reliability and large uncertainties, particularly in fault systems with massive earthquakes and long seismic gaps, i.e., long times without large ruptures. Here, we present a methodology that lays the groundwork to address these two limitations by proposing a framework for parameter estimation for a new complex earthquake model and investigating the potential benefits of supplementing sparse historical catalogs with synthetic catalogs.

Synthetic catalogs are becoming widely available through computer simulations based on rigorous physics-based models. These models can represent multiple earthquake rupture cycles using modern rock fracture models and efficient computational tools (Luo et al., 2017; Richards-Dinger and Dieterich, 2012). At present, the rate and state friction law (Dieterich, 1979; Ruina, 1983; Marone, 1998) is the canonical model for simulating such cycles. The state and friction law have enabled researchers to reproduce complex fault rheologies and earthquake rupture behaviors such as nucleation (Galvez et al., 2014), earthquake swarms (Lohman and McGuire, 2007), aftershocks (Dieterich and Kilgore, 1994), postseismic relaxation (Savage and Langbein, 2008), and coseismic, interseismic and postseismic strain and stress cycles (Barbot et al., 2012).

This paper formulates a framework to enlarge historical catalogs that have insufficient earthquake data with synthetic catalogs through a proposed parameter estimation technique. The technique is formulated for the model presented by Ceferino et al. (2020) and is based on two-step Bayesian update that utilizes a synthetic catalog to perform an initial parameter update followed by a second update using the historical catalog. The technique is solved with a Markov Chain Monte Carlo (MCMC) algorithm, and it is applied to the subduction zone along the coast of Lima, Peru. We use multiple physics-based synthetic catalogs, which we develop using quasi-dynamic earthquake cycle modeling based on the rate-and-state friction law (Rubin and Ampuero, 2005; Ampuero and Rubin, 2008). A formulation presented in this paper allows us to propagate the uncertainty in the synthetic catalogs to the parameter estimates. Finally, the paper evaluates the implications of including synthetic catalogs to determine large-earthquake recurrence and time-dependent seismic hazard in the region.

PROBABILISTIC MODEL

Ceferino et al. (2020, 2017) presented a probabilistic formulation for modeling time and space interactions between earthquake mainshocks. The following subsections briefly describe the earthquake rupture model for completeness.

Fault and rupture representation

The model represents the contact surface between tectonic plates as a plane subdivided into smaller area sections. Figure 1 shows the fault geometry, the sections, and an earthquake rupture (in shaded areas) occurring at time t. N is the total number of sections in the fault, and t is a discrete time index with time steps of one year. A rupture at year t is represented by the rupture vector $\boldsymbol{X_t} \in \{0,1\}^N$. Each section has a corresponding element $X_t(j)$ of the vector $\boldsymbol{X_t}$, representing its rupture state, where $X_t(j) = 1$ if section j was involved in a rupture at year t, or 0 otherwise. A vector $\boldsymbol{T_t} \in \mathbb{N}^N$ contains the times since the last earthquake at year t for each section. Consequently, the element $T_t(j)$ of the vector $\boldsymbol{T_t}$

represents the number of years since the last rupture until year t in section j. $T_t(j)$ is updated according to whether there was a rupture in the specific section j during year t. If there is a rupture in section j at year t (i.e., $X_t(j) = 1$), then the time $T_{t+1}(j)$ resets to 1 at time $t + 1$. Otherwise, the time since the last rupture increases by one unit, $T_{t+1}(j) = T_t(j) + 1$. This is represented in the following equation:

$$T_{t+1}(j) = (T_t(j))(1 - X_t(j)) + 1 \tag{1}$$

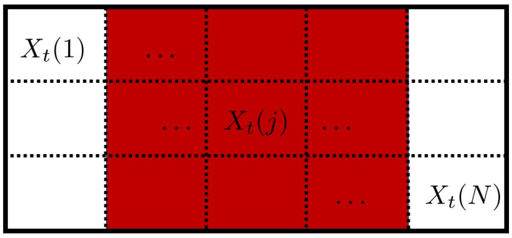

Figure 1: Fault subdivision into small sections. The shaded sections represent a rupture at year t. Extracted from Ceferino et al. (2020)

Probabilistic model formulation

The rupture occurrence at year t conditioned on the time since the last earthquake, i.e., $\boldsymbol{X_t}|\boldsymbol{T_t}$, is modeled as a multivariate Bernoulli distribution:

$$\boldsymbol{X_t}|\boldsymbol{T_t} \sim \text{Multivariate Bernoulli}(\boldsymbol{p_t}, \boldsymbol{\Sigma}) \tag{2}$$

where $\boldsymbol{p_t}$ is the vector containing the rupture occurrence probabilities of the N sections, and $\boldsymbol{\Sigma}$ is the covariance matrix of size $N \times N$ containing rupture correlations between the sections. The vector's element $p_t(j)$ is a function of the time since the last rupture $T_t(j)$ at the j-th section. $p_t(j)$ can be estimated as

$$p_t(j) = P[X_t(j) = 1|T_t(j)] = P[T_t(j) + 1 \geq \tau_j|\tau_j > T_t(j)] \tag{3}$$

where τ_j is a random variable that represents the rupture interevent time of the j-th section. τ_j is modeled as a BPT distribution, whose probability density function (pdf) is

$$f_{\tau_j}(t) = \Big(\frac{\mu_j}{2\pi\alpha_j t^3}\Big)^{1/2} \exp\Big(-\frac{(t-\mu_j)^2}{2\mu_j\alpha_j^2 t}\Big) \tag{4}$$

μ_j and α_j are the mean and coefficient of variation (aperiodicity) of τ_j, respectively. Tweedie (1957); Chhikara and Folks (1977) provide comprehensive descriptions of the properties of the BPT distribution. According to these studies, the cumulative density function (CDF) of a BPT distribution is

$$F_{\tau_j}(t) = P[\tau_j \leq t] = \Phi[u_1(t)] + e^{2/\alpha_j^2}\Phi[-u_2(t)] \tag{5a}$$

$$u_1(t) = \alpha_j^{-1}[t^{1/2}\mu_j^{-1/2} - t^{-1/2}\mu_j^{1/2}] \tag{5b}$$

$$u_2(t) = \alpha_j^{-1}[t^{1/2}\mu_j^{-1/2} + t^{-1/2}\mu_j^{1/2}] \tag{5c}$$

where $\Phi[.]$ is a cumulative function of a standard normal distribution. Using the Bayes rule, $p_t(j)$ can be estimated as

$$p_t(j) = \frac{(\Phi[u_1(T_t(j))] - \Phi[u_1(T_t(j)-1)]) + e^{2/\alpha_j^2}(\Phi[-u_2(T_t(j))] - \Phi[-u_2(T_t(j)-1])}{1 - (\Phi[u_1(T_t(j)-1)] + e^{2/\alpha_j^2}\Phi[-u_2(T_t(j)-1)])} \tag{6}$$

The elements $\rho_{i,j}$ of the covariance matrix $\boldsymbol{\Sigma}$ are defined by a spherical correlogram in order to capture earthquake nucleation and spatial rupture propagation effects. The correlogram is

$$\rho_{i,j} = \exp\Big(-\Big(\frac{dist(i,j)}{\gamma}\Big)^2\Big) \tag{7}$$

The correlation decreases as function of the distance $dist(i,j)$ between the sections i and j, with a characteristic correlation length γ.

Copulas method

Because correlated multivariate Bernoulli distributions cannot be written in closed-form, an approximation is used through the copula method (Jin et al., 2015). A vector $\boldsymbol{Z_t}$ of normally distributed random variables is first defined, with a zero-valued mean vector and a covariance equal to the covariance matrix $\boldsymbol{\Sigma}$ (i.e., from the correlogram in Equation 7). Then, $X_t(j)$ is obtained by evaluating whether $\Phi[Z_t(j)]$ is smaller than $p_t(j)$, as

$$X_t(j) = \begin{cases} 1 & \text{if } \Phi[Z_t(j)] < p_t(j) \\ 0 & \text{otherwise} \end{cases} \tag{8}$$

BAYESIAN PARAMETER ESTIMATION PROCEDURE

Ceferino et al. (2020) described a simple parameter estimation method for the probabilistic model summarized thus far. The method uses Maximum Likelihood Estimation (MLE) at each individual fault section separately to estimate μ_j and α_j. Then, the method calibrates γ to match annual exceedance rates and average seismic moment releases in tectonic faults. This method was applied to the subduction zone along the coast of Lima, Peru, due to its implementation simplicity. However, Ceferino et al. (2018) showed that this method can generate unreliable estimates of rupture occurrence, particularly, when earthquake rupture data is sparse.

In this paper, we propose an improved parameter estimation technique. It uses a Bayesian update, which unlike the technique proposed in Ceferino et al. (2020), it updates all the parameters simultaneously rather than separately. This feature gives more reliable parameter estimates, particularly, for the fault sections with few or no known earthquake ruptures (Ceferino et al., 2018). In addition, we propose a two-step Bayesian update, which is illustrated in a plot in Data and Resources. In the first Bayesian update, the prior distributions of the parameters are defined as independent, lognormally distributed random variables. The prior distribution hyperparameters can be chosen by a combination of expert opinion, existing common BPT parameter values for similar tectonic regions (Sykes and Menke, 2006), or average historical earthquake interevent times in neighboring region. The lognormal distribution can work as a weakly informative distribution, which enables to use the prior variances for hyperparameter regularization when the data are sparse (Hamra et al., 2013). Then, the technique updates the parameters of the model to a posterior joint distribution using the physics-based catalog. The posterior is estimated using a MCMC technique as described later. For simplicity, in the second Bayesian update, the prior distributions of the parameters are also assumed to be independent, lognormally distributed random variables. Then, the lognormal distributions' hyperparameters are estimated using MLE on the realizations sampled from the MCMC of the first Bayesian update. Finally, the final posterior of the parameters is estimated using the MCMC and the historical earthquake catalog. As a result, the physics-based simulated earthquake catalog calibrates the prior that is later combined with the historical catalog in the second update. The following subsection describes the Bayesian update formulation and the MCMC technique.

Bayesian update

There are $2 \times N + 1$ parameters in the model, two parameters per each of the N sections of the fault (α_j and μ_j), and another parameter defining the correlogram model (γ).

Posterior

The Bayesian update for the posterior distribution of the parameters is formulated as

$$P(\boldsymbol{\alpha}, \boldsymbol{\mu}, \gamma | \boldsymbol{\Psi}) \propto P(\boldsymbol{\Psi} | \boldsymbol{\alpha}, \boldsymbol{\mu}, \gamma) P(\boldsymbol{\alpha}, \boldsymbol{\mu}, \gamma) \tag{9}$$

The posterior is proportional to the likelihood of observing the data, $P(\boldsymbol{\Psi}|\boldsymbol{\alpha}, \boldsymbol{\mu}, \gamma)$, times the prior distribution of the parameters, $P(\boldsymbol{\alpha}, \boldsymbol{\mu}, \gamma)$. $\boldsymbol{\Psi}$ represents the collection of K years of rupture history in the earthquake catalog for all the fault sections: $\boldsymbol{\Psi} = \{\boldsymbol{X_1}, \boldsymbol{X_2}, \ldots, \boldsymbol{X_K}\}$. The vectors $\boldsymbol{\alpha}$ and $\boldsymbol{\mu}$ are the collections of α_j and μ_j, respectively, for all the fault sections.

Prior

The prior distributions are assumed to be lognormal because of its mathematical simplicity and its ability to represent μ_j, α_j and γ as positive numbers. Other distributions that are restricted to positive numbers and which are believed to represent the distribution of the parameters reasonably well could also be used. The parameters' marginal probability distributions are

$$\alpha_j \sim P[\alpha_j] : \text{Lognormal}(\mu_{\log \alpha_j}, \sigma_{\log \alpha_j}) \tag{10}$$

$$\mu_j \sim P[\mu_j] : \text{Lognormal}(\mu_{\log \mu_j}, \sigma_{\log \mu_j}) \tag{11}$$

$$\gamma \sim P[\gamma] : \text{Lognormal}(\mu_{\log \gamma}, \sigma_{\log \gamma}) \tag{12}$$

where the prior distributions are defined by the corresponding logarithmic mean and standard deviation (SD) of the lognormal distribution. We assume the parameters to be independent in the prior distribution, thus the joint probability distribution can be written as

$$P(\boldsymbol{\alpha}, \boldsymbol{\mu}, \gamma) = P[\gamma] \prod_{j=1}^{N} P[\mu_j] P[\alpha_j] \tag{13}$$

Likelihood of observing the data

The likelihood of observing the rupture history, $P[\boldsymbol{\Psi}|\boldsymbol{\alpha}, \boldsymbol{\mu}, \gamma]$, can be computed using the following formulation. The rupture history $\boldsymbol{\Psi}$ is initially conditioned by $\boldsymbol{T_1}$, the number of years since the last earthquake at the starting year of the catalog. Given that $\boldsymbol{T_{t+1}}$ is a deterministic function of $\boldsymbol{T_t}$ and $\boldsymbol{X_t}$ and there is a one-to-one correspondence between $\boldsymbol{T_{t+1}}$ and $\{\boldsymbol{T_t}, \boldsymbol{X_t}\}$ (see Equation 1), then

$$P[\boldsymbol{\Psi}|\boldsymbol{\alpha}, \boldsymbol{\mu}, \gamma] = P_{\boldsymbol{\alpha},\boldsymbol{\mu},\gamma}[\boldsymbol{X_1}, \boldsymbol{X_2}, \cdots, \boldsymbol{X_H}|\boldsymbol{T_1}] = P[\boldsymbol{X_1}, \boldsymbol{T_2}, \boldsymbol{X_2}, \cdots, \boldsymbol{T_H}, \boldsymbol{X_H}|\boldsymbol{T_1}] \tag{14}$$

In addition, the set $\{\boldsymbol{T_{t+1}}, \boldsymbol{X_t}\}$ is a Markov chain (MC) because if $\{\boldsymbol{T_{t+1}}, \boldsymbol{X_t}\}$ is conditioned on the last step $\{\boldsymbol{T_t}, \boldsymbol{X_{t-1}}\}$, it is independent of all the previous rupture history. This is because the set $\{\boldsymbol{T_t}, \boldsymbol{X_{t-1}}\}$ contains all the required information to assess the rupture in the next year, i.e., whether a rupture occurred the previous year and the time since the last rupture in each fault section. Therefore

$$P[\boldsymbol{\Psi}|\boldsymbol{\alpha}, \boldsymbol{\mu}, \gamma] = P_{\boldsymbol{\alpha},\boldsymbol{\mu},\gamma}[\boldsymbol{T_2}, \boldsymbol{X_1}|\boldsymbol{T_1}] \prod_{t=2}^{H} P_{\boldsymbol{\alpha},\boldsymbol{\mu},\gamma}[\boldsymbol{T_{t+1}}, \boldsymbol{X_t}|\boldsymbol{T_t}, \boldsymbol{X_{t-1}}] \tag{15}$$

Finally, given the one-to-one correspondence between $\boldsymbol{T_{t+1}}$ and $\{\boldsymbol{T_t}, \boldsymbol{X_t}\}$ described previously, $\boldsymbol{T_{t+1}}$ can be dropped from the conditional probabilities. $\boldsymbol{X_{t-1}}$ can also be dropped from the conditional set $\{\boldsymbol{T_t}, \boldsymbol{X_{t-1}}\}$, because $\boldsymbol{T_t}$, the time since the last rupture in each section, is the only information that is needed to evaluate the likelihood of $\boldsymbol{X_t}$ (see Equation 2). Thus

$$P[\boldsymbol{\Psi}|\boldsymbol{\alpha}, \boldsymbol{\mu}, \gamma] = P_{\boldsymbol{\alpha},\boldsymbol{\mu},\gamma}[\boldsymbol{X_1}|\boldsymbol{T_1}] \prod_{t=2}^{H} P_{\boldsymbol{\alpha},\boldsymbol{\mu},\gamma}[\boldsymbol{X_t}|\boldsymbol{T_t}] \tag{16}$$

We evaluate $P_{\boldsymbol{\alpha},\boldsymbol{\mu},\gamma}[\boldsymbol{X_t}|\boldsymbol{T_t}]$ using the copula method described earlier. $P_{\boldsymbol{\alpha},\boldsymbol{\mu},\gamma}[\boldsymbol{X_t}|\boldsymbol{T_t}]$ is estimated as the probability that the vector $\boldsymbol{Z_t}$ (from Equation 8) is within the region defined in Equation 17

$$P_{\boldsymbol{\alpha},\boldsymbol{\mu},\gamma}[\boldsymbol{X_t}|\boldsymbol{T_t}] = P[\cap_{j=1}^{N} A_j], \text{where} \begin{cases} A_j = \{Z_t(j) \leq \Phi^{-1}[p_t(j)]\} \text{ if } X_t(j) = 1, \\ \text{or } A_j = \{Z_t(j) > \Phi^{-1}[p_t(j)]\} \text{ otherwise} \end{cases} \tag{17}$$

where $Z_t(j)$ is the j-th element of the vector $\boldsymbol{Z_t}$ that follows a normal distribution. This region is the intersection of the regions A_j, where A_j extends over the region $\{Z_t(j) \leq \Phi^{-1}[p_t(j)]\}$ if there is a rupture in the j-th section at year t, or extends over the region $\{Z_t(j) > \Phi^{-1}[p_t(j)]\}$ otherwise.

Posterior Estimation using Markov Chain Monte Carlo

To fully evaluate the posterior distribution, a normalizing factor must be estimated so that the integral of the distribution over the entire parameter space is 1 (Equation 9). However, because of the complexity and high dimensionality of the posterior distribution, it is not feasible to find the solution in closed form. To overcome this issue, we use the MCMC technique to find the posterior as it allows us to sample from and evaluate complex, high-dimensional distributions (Liu, 2004), avoiding the numerical challenges stemming from the highly dimensional integration.

We used the Metropolis-Hastings (MH) algorithm, a version of MCMC. The MH MCMC searches on the high-dimensional parameter space using a MC whose stationary distribution is the posterior distribution of the parameters (see in Data and Resources). In order to generate a new parameter sample $[\boldsymbol{\alpha}, \boldsymbol{\mu}, \gamma]_m$, we estimate a sample candidate $[\boldsymbol{\alpha}, \boldsymbol{\mu}, \gamma]^*$ using a random walk with an uncorrelated multivariate normal distribution

$$[\boldsymbol{\alpha}, \boldsymbol{\mu}, \gamma]^* \sim Q([\boldsymbol{\alpha}, \boldsymbol{\mu}, \gamma] | [\boldsymbol{\alpha}, \boldsymbol{\mu}, \gamma]_{m-1}) = \mathcal{N}([\boldsymbol{\alpha}, \boldsymbol{\mu}, \gamma]_{m-1}, \mathrm{diag}([\boldsymbol{\sigma}^{\mathbf{2}}_{\boldsymbol{\alpha}}, \boldsymbol{\sigma}^{\mathbf{2}}_{\boldsymbol{\mu}}, \sigma^2_\gamma])) \tag{18}$$

In the random walk, the distribution of the next step, $Q([\boldsymbol{\alpha}, \boldsymbol{\mu}, \gamma] | [\boldsymbol{\alpha}, \boldsymbol{\mu}, \gamma]_{m-1})$, is a normal distribution with a mean that equals the values from parameter sample in the last step and with a covariance matrix that equals a diagonal matrix $\mathrm{diag}([\boldsymbol{\sigma}^{\mathbf{2}}_{\boldsymbol{\alpha}}, \boldsymbol{\sigma}^{\mathbf{2}}_{\boldsymbol{\mu}}, \sigma^2_\gamma])$, i.e., the walk has fixed variances in all parameters at each step. Then, we estimate an acceptance rate A as

$$A = \frac{P([\boldsymbol{\alpha}, \boldsymbol{\mu}, \gamma]^* | \boldsymbol{\Psi}) \times Q([\boldsymbol{\alpha}, \boldsymbol{\mu}, \gamma]^* | [\boldsymbol{\alpha}, \boldsymbol{\mu}, \gamma]_{m-1})}{P([\boldsymbol{\alpha}, \boldsymbol{\mu}, \gamma]_{m-1} | \boldsymbol{X}) \times Q([\boldsymbol{\alpha}, \boldsymbol{\mu}, \gamma]_{m-1} | [\boldsymbol{\alpha}, \boldsymbol{\mu}, \gamma]^*)} \tag{19}$$

where $P([\boldsymbol{\alpha}, \boldsymbol{\mu}, \gamma] | \boldsymbol{\Psi})$ is the posterior distribution that can be estimated with Equation 9. Because the random walk has symmetrical probabilities, $Q([\boldsymbol{\alpha}, \boldsymbol{\mu}, \gamma]_{m-1} | [\boldsymbol{\alpha}, \boldsymbol{\mu}, \gamma]^*) = Q([\boldsymbol{\alpha}, \boldsymbol{\mu}, \gamma]^* | [\boldsymbol{\alpha}, \boldsymbol{\mu}, \gamma]_{m-1})$. Thus

$$A = \frac{P([\boldsymbol{\alpha}, \boldsymbol{\mu}, \gamma]^* | \boldsymbol{\Psi})}{P([\boldsymbol{\alpha}, \boldsymbol{\mu}, \gamma]_{m-1} | \boldsymbol{\Psi})} \tag{20}$$

Using Equation 9, the acceptance rate A can be estimated as a function of the prior distribution and the likelihood of observing the data

$$A = \frac{P(\boldsymbol{\Psi} | [\boldsymbol{\alpha}, \boldsymbol{\mu}, \gamma]^*) P([\boldsymbol{\alpha}, \boldsymbol{\mu}, \gamma]^*)}{P(\boldsymbol{\Psi} | [\boldsymbol{\alpha}, \boldsymbol{\mu}, \gamma]_{m-1}) P([\boldsymbol{\alpha}, \boldsymbol{\mu}, \gamma]_{m-1})} \tag{21}$$

Finally, the sample candidate is accepted with probability A. According to the MH properties, the samples will eventually converge to the posterior distribution of the parameters when the MC reaches stationarity. Therefore, the first B samples belong to the burn-in period and are discarded. If M is the total number of samples with the MCMC technique, then only $M - B$ samples are used to evaluate the posterior distribution.

COMBINING MULTIPLE SYNTHETIC CATALOGS

Synthetic catalogs result from physics-based models, e.g., friction laws, defined by parameters that have not been directly measured at the fault interface. Thus, it is critical to account for the uncertainty in the estimates of physics-based models' parameters. Understanding these sources of uncertainty and quantifying how they interact with historical earthquake data is critical for combining physics-based simulations and historical catalogs.

Through simulations, we expect that modeler will obtain multiple synthetic rupture histories $\boldsymbol{\Psi}_{\mathbf{s}}$, where $s \in \mathbf{S} : \{1, \ldots, S\}$ and S is the number of different synthetic catalogs, which incorporate uncertainty from the physics-based model. Assuming independence between the true (historical) rupture history $\boldsymbol{\Psi}_{\mathbf{H}}$ and the synthetic data history, then the two-step parameter distributions $P(\boldsymbol{\alpha}, \boldsymbol{\mu}, \gamma | \boldsymbol{\Psi}_{\mathbf{H}}, \boldsymbol{\Psi}_{\mathbf{s}})$ can be combined to propagate the uncertainty in the synthetic catalogs to the final parameter estimates as

$$P_{\mathbf{S}}(\boldsymbol{\alpha}, \boldsymbol{\mu}, \gamma | \boldsymbol{\Psi}_{\mathbf{H}}) = \sum_{\mathbf{s} \in \mathbf{S}} P(\boldsymbol{\alpha}, \boldsymbol{\mu}, \gamma | \boldsymbol{\Psi}_{\mathbf{H}}, \boldsymbol{\Psi}_{\mathbf{s}}) P(\boldsymbol{\Psi}_{\mathbf{s}}) \tag{22}$$

where $P(\boldsymbol{\Psi}_{\mathbf{s}})$ is the probability that each $\boldsymbol{\Psi}_{\mathbf{s}}$ is representative of the fault's seismitectonic features. We propose to estimate $\boldsymbol{\Psi}_{\mathbf{s}}$ as

$$P(\mathbf{\Psi_s}) \propto f(\epsilon_{\mathrm{ISC}}) \times f(\Delta\tau) \tag{23}$$

where $f(\epsilon_{\mathrm{ISC}})$ is a normal pdf of interseismic coupling, and ϵ_{ISC} can be estimated as the root mean square (RMS) of the difference between ISC in $\mathbf{\Psi_s}$ and fault's average GPS-inferred ISC. $f(\Delta\tau)$ is a lognormal pdf of median shear stress drops in the fault (Allmann and Shearer, 2009), and $\Delta\tau$ can be estimated from the earthquakes in $\mathbf{\Psi_s}$.

MODEL SETUP AND EARTHQUAKE DATA

The parameter estimation technique was applied to the central portion of the subduction zone of Peru, where the oceanic Nazca plate is subducting beneath the continental South American plate at an average rate of 6 cm/yr (Kendrick et al., 2003). Figure 2 shows the seismotectonic setting of the region of analysis and the rupture areas of the four last large earthquakes that occurred in 1940, 1966, 1970, and 1974. According to historical reports and instrumental catalogs, the region has been very active and has generated multiple large earthquakes in the last 450 years (Villegas-Lanza et al., 2016). This region has a size of 650 km along the strike direction, 200 km along the dip direction, and a dip angle of 15^o, reaching depths of up to 50 km. The northern and southern boundaries of the selected seismic region correspond to the areas of significant fault creep inferred by Villegas-Lanza et al. (2016) using geodetic data.

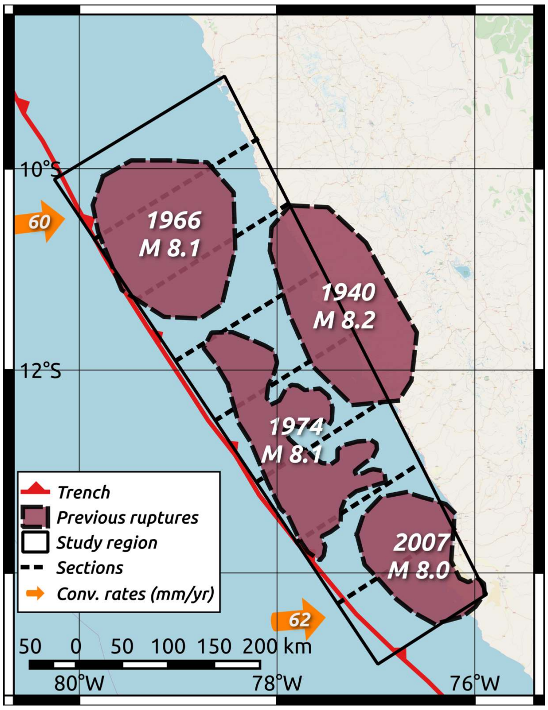

Figure 2: Central Peru subduction zone and its recent seismicity. The line parallel to the coastline shows the fault trench where the Nazca and South American plates converge. The black quadrilateral shows the region of study subdivided into eight sections, and the four enclosed areas show the rupture areas of the four most recent large earthquakes, with the year and magnitude indicated in each area. The arrows indicate the plate convergence rates in mm/year. Modified from Ceferino et al. (2020)

The tectonic region was discretized into eight sections along the strike direction so that the rupture of an individual section represents an earthquake of magnitude 7.5. Because the fault sections represent the minimum tectonic area unit, the model only will capture large earthquakes with magnitude equal to or larger than 7.5. The eight sections are shown by the dashed lines in Figure 2. In this application, the model has 17 parameters: one μ_j and α_j per each section, and γ for the correlogram. The sections are labeled from 1 to 8 starting from south to north.

The following subsections describe the earthquake data used in the two-step parameter estimation in the study region.

Historical Catalog

We used the historical catalog compiled by Ceferino et al. (2020). Additionally, we included in the catalog two earthquakes that occurred in 1806 and 1828, respectively. Although several studies omit these two earthquakes, Silgado (1978) and Seiner (2011) showed that they were large and catastrophic events, and Villegas-Lanza et al. (2016) estimated the their magnitudes were of 7.5.

Next, we projected all rupture areas along the strike direction and discretized them to match the fault sections defined in Figure 2 (see discussion about discretization in Ceferino et al. (2020)). Figure 3 shows these rupture projections in the Y axis and the earthquake occurrence year in the X axis.

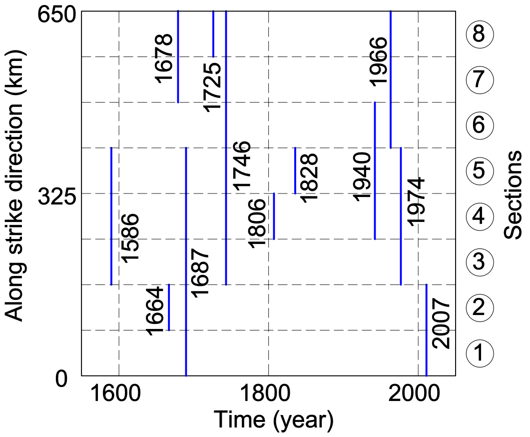

Figure 3: Along-strike distribution of historical earthquake ruptures through time. The rupture lengths were discretized to match the fault sections.

Synthetic Catalog Using Physics-based Simulation

We generated synthetic catalogs of seismic events using a physics-based model for earthquake cycles. In this model, the tectonic load resulting from the convergence between plates and fault slip is balanced by a fault friction resistance governed by the rate-and-state friction law (Dieterich, 1979; Tullis, 1988; Marone and Kilgoret, 1993). The black solid line in Figure 2 represents the fault interface as a 2D frictional plane embedded in a 3D elastic medium dipping 15°(Hayes et al., 2018). As a result of the tectonic load, some regions on the fault become unstable, nucleate and trigger earthquakes of different magnitudes (Rubin and Ampuero, 2005). We used the implementation in the software QDYN to carry out the physics-based modeling (Luo et al., 2017). The implementation uses adaptive time steps for earthquake cycle modeling (Ampuero and Rubin, 2008). The time steps vary from 10^{-6} s during the coseismic period to 10^{3} s during the interseismic period. To limit computational cost, this physics-based model has simplifying assumptions, like the use of rate-and-state friction even during fast sliding stages. However, it maintains the advantage of tracking the stress history on the fault, accounting for the quasi-static elastic interactions between asperities mediated by co-seismic stress transfer and intervening transient creep, and utilizing it to compute the evolution of the future earthquakes.

Fault asperities

We represent the main fault asperities that produce earthquakes by assigning heterogeneous fault friction properties defining four velocity-weakening (VW) regions on the fault as shown in Figure 4. These VW regions are locked in the interseismic period between earthquakes (Kaneko et al., 2010). Based on analysis of geodetic data, Villegas-Lanza et al. (2016) found that regions of high locking ratio overlap with the regions of historical ruptures. The rupture geometries of large earthquakes before 1940 are not available in detail, only estimates of their extension along strike. Nevertheless, this limited information is consistent with ruptures before 1940 occurring on the same four large asperities as the events after 1940. Overall, the information available suggests that the velocity weakening areas persist in time. Strong spatial correlations between high interseismic coupling areas and rupture areas of historical earthquakes have been observed on several subduction zones such as the Kurile-Japan trench (Ito et al., 2000) and offshore of Sumatra (Konca et al., 2007; Chlieh et al., 2008).

The shapes of the VW regions were idealized as ellipses with length L_{asp} along the strike direction and width W_{asp} along the dip direction. They were located according to the rupture areas of the last four large earthquakes shown in Figure 2. We assume that these previous large rupture areas revealed the main asperities.

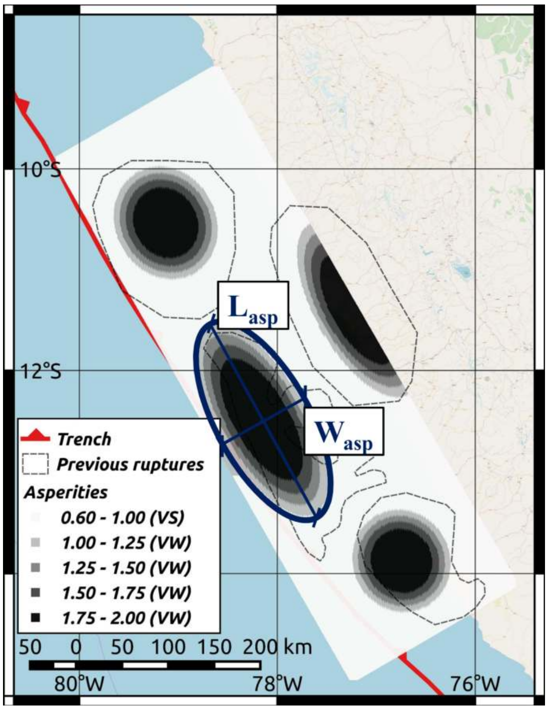

Figure 4: Distribution of asperity regions in the physics-based model. The shaded, rectangular area represents the extent of the 2D frictional area. Its size is 650 km along the strike direction and 200 km along the dip direction. The four VW asperity regions with high interseismic coupling are represented by ellipses with length L_{asp} along the strike direction and W_{asp} along the dip direction and are shown in dark shades. The larger the dimensions of L_{asp} and W_{asp}, the closer the VW regions are to each other. The VS areas are shown in a white shade. The grey scale indicates the b/a ratio of the rate-and-state friction law.

Input data for the physics-based model

We set the reference steady-state slip velocity equal to 6 cm/year, which is the convergence rate of the tectonic plates (Villegas-Lanza et al., 2016). Other input data were defined according to commonly used values in previous studies in subduction zone regions (Liu and Rice, 2007). The values are fully reported in Data and Resources. We verified that the input data corresponded to the values found in laboratory experiments. For example, the reference frictional coefficient f of 0.6 is within the ranges from 0.5 to 0.8 of frictional coefficients found for most materials (Dieterich and Kilgore, 1994). Similarly, the values of the direct-effect frictional coefficient a and the state-effect frictional coefficient b often vary within between 0.005 and 0.015 in rocks (Dieterich and Kilgore, 1994). The selected values of a and b in our case study range from $\sim$0.0015 to 0.0085. Part of this range is lower than the laboratory values in order to have stress drops consistent with empirical observations and to handle computations constraints as explained subsequently. We assume that these values are constant through the entire fault, except for the state-effect frictional coefficient b. The sign of the difference between b and the direct-effect frictional coefficient a determines whether a region has VW behavior ($b - a > 0$) or velocity-strengthening (VS) behavior ($b - a < 0$). The VS regions tend to creep and do not nucleate earthquakes, but the areas of partial interseismic locking generally extend out of the VW areas into the VS areas (Kaneko et al., 2010). In order to have smoothness, we applied an exponential spatial transition of b values between the VW and VS regions.

We tested multiple values of a, b, and characteristic slip distance D_c, under the following constraints. The parameter $b-a$ in the VW regions controls the stress drop during earthquakes. It directly influences the earthquake magnitude and frequency distribution in the simulation. The ratio D_c/b controls the required minimum mesh size in the simulation, as described in the next section. These parameters were varied in order to ensure that the results capture the main features of the previous seismicity and satisfy computational constraints. Table 1 shows the three cases that best represented the seismicity in the region while capturing different possible earthquake behaviors.

Table 1: Values of a, b and D_c for the three selected models.

Input Data	Case A	Case B	Case C
a	0.0014	0.0028	0.0042
b (VS)	0.0008	0.0017	0.0025
b (VW)	0.0028	0.0056	0.0084
D_c	2.3 cm	4.6 cm	6.8 cm

Computational constraints

The physics-based model is computationally demanding both in terms of memory usage and execution time. The software QDYN uses the Message Passing Interface (MPI) and Fast Fourier Transform (FFT) methods to compute matrix multiplications efficiently and track stresses and slips in the fault at each time step. We utilized 256 processors of the Stanford Sherlock computer cluster. The computational time increases significantly with reduced grid sizes. The model running time was approximately seven days for the grid size shown in Data and Resources for 2,000 years of simulation. In order to have a sound physics-based model, the model parameters in this application were set up according to the two following constraints.

First, the grid sizes dl and dw along the strike and dip directions, respectively, were set such that they were at least three times smaller than the cohesive zone length (Day et al., 2005; Lapusta and Liu, 2009). The cohesive zone length is comparable to $L_b = \frac{G' D_c}{\sigma b}$, where G' is the shear modulus for anti-plane rupture, and equal to the shear modulus G divided by one minus the Poisson's ratio for in-plane rupture. The values of G, D_c, σ, and b are shown in Data and Resources. Because b is larger in the VW regions, these regions impose heavier constraints on the grid size than the VS regions. We chose grid sizes such that $dl/L_b \approx 0.3$ and $dw/L_b \approx 0.25$. Either decreasing the grid sizes or increasing L_b would have resulted in smaller ratios. However, computational constraints did not allow us to further decrease the grid sizes, and the second model constraint described in the next paragraph did not allow us to increase L_b. Implementations that use the hierarchical matrix method could enable simulations with smaller grid size (Bradley, 2014).

Second, the dimensions of VW regions, L_{asp} and W_{asp}, were set such that they were significantly larger than the nucleation length $L_\infty = \frac{L_b}{\pi}\left(\frac{b}{b-a}\right)^2$ (Ampuero and Rubin, 2008). Here, L_{asp}/L_∞ and W_{asp}/L_∞ range from 35 to 80 for all VW regions. Smaller ratios can result in simulations with spurious earthquake ruptures that break all asperities in each event. Thus, the ratios were not further reduced, and L_b could not be increased.

Sensitivity to the asperity size

The sensitivity to different asperity sizes was analyzed by varying the sizes and locations of the four VW regions, which were labeled according to the location of their associated previous rupture. First, the VW regions' centers were located at the rupture areas' centroids. Then, the ellipses' locations and sizes were varied until the simulated interseismic coupling (ISC) areas matched the results inferred from recent GPS measurements of crustal motions (Villegas-Lanza et al., 2016) as will be described later. In this paper, three representative cases with VW centers but different sizes are presented (Table 2). The ellipses' diameters of cases 2 and 3 are 90% and 80% of the diameters of case 1, respectively, to show the effect of varying asperity sizes. Figure 4 shows the extent of the VW regions for case 2.

Validity of the physics-based synthetic catalogs

In this subsection, we present the results of the physics-based simulation for the cases A-1, A-2, A-3, B-1, B-2, B-3, C-1, C-2 and C-3. Each case represents a different selection of the values of two ingredients of the physics-based model: friction properties and asperity sizes. For example, case B-2 has values of a, b, and D_c according to case B in Table 1 and asperity sizes according to case 2 in Table 2. We selected these cases to represent a broad set of feasible earthquake behaviors in the physics-based simulation.

Table 2: Three representative asperity sizes tested in the model calibration. Lengths are provided in km.

Asperity	Center		Case 1		Case 2		Case 3	
	lat	lon	L_{asp}	W_{asp}	L_{asp}	W_{asp}	L_{asp}	W_{asp}
1940	-77.22°	-11.42°	255	115	229	104	204	92
1966	-79.16°	-10.57°	150	135	135	122	120	108
1974	-78.20°	-12.51°	280	118	252	107	224	107
2007	-76.79°	-13.91°	133	128	119	116	106	102

The physics-based simulation outputs instantaneous slip rate throughout the fault over the 2,000 years of simulation. During nucleation the slip rate increases significantly and reaches values above 0.1 m/s during the coseismic phase. We define the beginning of an earthquake when the slip rate at any point exceeds 1.6 cm/s. This threshold value is 10% of the slip rate at which inertial effects (radiation damping) start to dominate (Rubin and Ampuero, 2005). While high slip rates propagate through the fault, the total earthquake slip accumulates in the rupture area. The earthquake is considered to be finished once all points have slip rates below 1.6 cm/s. The final earthquake area is estimated as the area where the final earthquake slip exceeded 10% of the maximum earthquake slip. For example, a plot in Data and Resources shows an earthquake rupture area from the simulation in case C-2. In this case the earthquake rupture area is 15,000 km^2, and the magnitude is 8.4. This earthquake occurs in the VW area 2007, where the 2007 Pisco earthquake occurred. This earthquake occurs in year 656 in the simulation, and its average stress drop is 2.8 MPa. Additionally, we obtained reasonable rupture areas and slips compared to historical earthquakes. A plot in Data and Resources shows an example of how the simulated earthquake rupture areas and slip distributions fall within the ranges found in empirical observations by Wells and Coppersmith (1994); Papazachos et al. (2004).

Figure 5 shows the synthetic catalogs for the 2000 years of simulation for the second approach for cases A-2, B-2, and C-2. Similar plots for the nine cases (A-1, A-2, A-3, B-1, B-2, B-3, C-1, C-2 and C-3) are included in Data and Resources. We observed that the simulated earthquakes in cases A, B, and C have different shear stress drops. We estimated stress drops as the difference between the shear stress at the end and start of each earthquake, spatially-averaged within its rupture area. The stress drops vary according to the values of b, a, and σ, roughly consistent with the expectation in rate-and-state friction models that stress drops are approximately proportional to $\sigma(b-a)$ (Ampuero and Rubin, 2008). According to the values in Table 1, the stress drops in case A should be half those in case B and a quarter of those in case C. In cases A-1, A-2 and A-3, the median drop was 0.64 MPa; in cases B-1, B-2 and B-3, the median drop was were 1.4 MPa; and in cases C-1, C-2 and C-3, the median drop was 2 MPa. After analyzing 860 historical earthquakes worldwide, Allmann and Shearer (2009) determined that in subduction zones the distribution of earthquake stress drops ranges from 0.3 to 30 MPa, with a median of 3 MPa worldwide that is consistent with the specific observations in the subduction fault along the coast of South America. These empirical observations also validate the suitability of the synthetic catalogs.

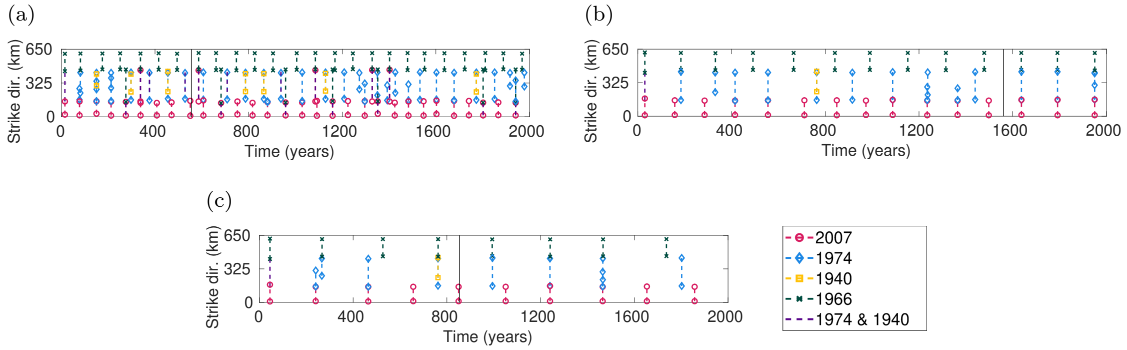

Figure 5: Physics-based synthetic earthquake catalogs for nine cases. Earthquake rupture lengths in the along-strike direction are shown as gray vertical lines at their time of occurrence. For each event, a symbol indicates which VW regions broke (see legend). (a) Case A-2, (b) Case B-2, and (c) Case C-2. The red vertical line in case B-2 indicates the snapshot time selected for the comparison of ISC ratios in Figure 6.

Finally, we verified that the snapshots of ISC in the synthetic catalog match the high-coupling regions inferred from GPS data. The ISC ratio at any point of the fault is defined as $(\nu - \nu_{ss})/\nu_{ss}$, where ν is the instantaneous slip rate and ν_{ss} is the steady-state (long-term) slip rate, which is the plate convergence rate. When the ISC ratio equals 0 there is total creep, and when the ISC ratio equals 1 there is full locking. Villegas-Lanza et al. (2016) utilized multiple GPS velocity measurements collected between 2008 and 2013 along the South American plate to infer spatially varying ISC through an inversion procedure. Figure 6a shows the mean ISC estimates from fitting the GPS data. There is a high ISC (> 0.75) area that extends laterally, roughly parallel to strike direction in the shallow part, from the southern region to two thirds of the fault's length. This area corresponds to the VW regions 1974 and 2007 of our model; however, it does not completely cover them. Moreover, the GPS-based ISC shows high ratios in the central east part of the fault where the VW region of 1940 is located.

The ISC varies over time as the fault undergoes multiple complex interactions between seismic and aseismic slips, and it heavily depends on the preceding earthquake cycles. Consequently, we sought earthquake cycles in the synthetic catalog that are similar to ones preceding the GPS data collection (before 2008). We selected snapshots in the physics-based simulations within the first five years after a large rupture in the southern sections that were preceded by ruptures in the central and northern sections in previous decades. These snapshots in Figure 6 and Supplementary Figure 6 show that the high-coupling regions have strong correspondence with the predefined VW regions, but extend beyond, i.e., larger VW regions have larger estimated areas with high ISC.

In contrast to the simulations, the GPS data shows a more irregular spatial distribution of ISC than the simulations. This discrepancy shows that the asperities in the fault have a more irregular spatial structure than the idealized ellipsoids in Figure 4. An application focused on capturing lower magnitudes would require an improvement in ISC matching at a finer spatial resolution to capture this spatial structure. Instead, in our application, we only verified that our matching results were acceptable on a coarser scale at the fault level by binning high and low ISC regions with a threshold of 0.5. We found that, on average, the synthetic data matched the GPS-inferred mean ISC predictions in 64% of the fault. Case B-1 and C-1 had the best performance matching GPS-inferred ISC in 69% of the fault.

Uncertainty in physics-based synthetic catalogs

Physics-based models generate synthetic catalogs that have uncertainty. From a Bayesian perspective, the physics-based model's inadequate definitions can lead to synthetic data with low probabilities of representing fault's seismicity. From a frequentist perspective, this would be equivalent to propagating "biases" in the synthetic data to the earthquake hazard. Thus, physics-based models need to be carefully defined. The last subsection described multiple synthetic-catalog features that can be used to validate the physics-based model, such as the distribution of slips, rupture areas, stress drops, and distributions of ISC. Here, we also show how they match historical moment magnitude distributions.

The nine synthetic catalogs exhibit variability in the exceedance rates through the entire magnitude range as a result of different input data (i.e., a, b, D_c) and varying asperity sizes as shown in Tables 1 and 2, respectively (Figure 7). By construction, the asperities in case 1 are more extensive and closer to each other than those in case 2, which are larger and closer than in case 3. As a result, earthquakes in case 1 are more likely to break neighboring asperities than in cases 2 and 3, generating earthquakes with larger magnitudes.

The historical catalog rates exhibit wide 95%-confidence intervals due to its short duration (Figure 7). For example, in our case study, only two earthquakes determine the exceedance rates for magnitudes larger than 8.2. As a result, the 95%-confidence interval is three times wider (relative to the mean exceedance rate) for magnitudes larger than 8.5 than for magnitudes close to 7.5 (see Data and Resources). We find that the use of multiple synthetic catalogs whose exceedance rates spread across these wide confidence intervals offers an opportunity to account for potentially feasible earthquake cycles not yet observed in the fault.

PARAMETER ESTIMATION APPLICATION

Here, we use the synthetic catalog to supplement the historical catalog using our proposed framework.

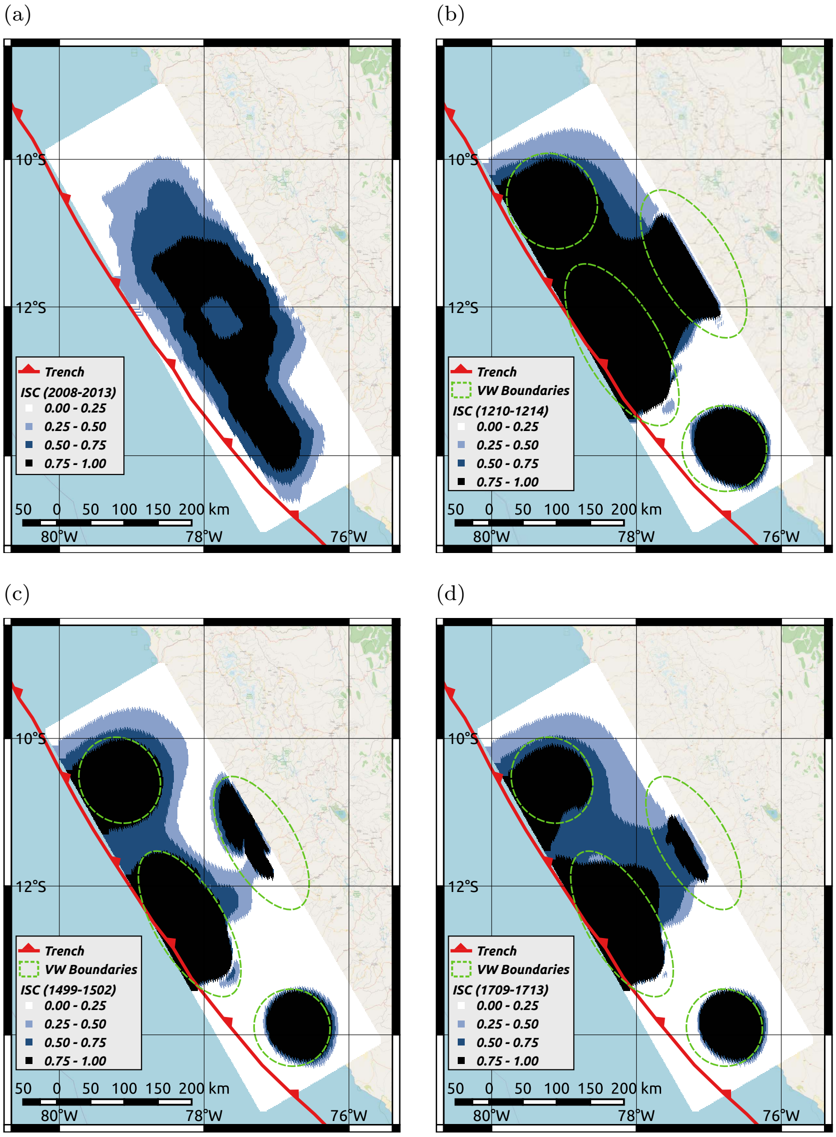

Figure 6: Comparison of observed and modeled ISC ratios. (a) ISC ratio inferred from GPS data collected from 2008 to 2013 (Villegas-Lanza et al. (2016)'s model 4.5). (b), (c) and (d) Synthetic ISC ratios from three physics-based simulations in cases B-1, B-2, and B-3, respectively. The simulation time intervals used to estimate synthetic ISC are indicated in parenthesis. The dashed ellipses show the boundaries of the VW asperity, defined by $b - a = 0$. High ISC areas can extend beyond the asperity boundaries.

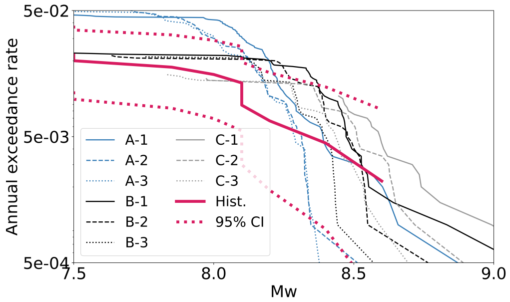

Figure 7: Annual magnitude exceedance rates from the synthetic and historical catalogs. The nine synthetic catalogs are shown in lighter and thinner lines. The rate mean estimates from the historical catalog are shown in the solid darker line, and its 95% confidence interval, estimated according to Ulm (1990), is shown in dashed lines. Similar confidence intervals can be calculated for each synthetic catalog, and they are less wide as a result of longer timespans. A plot in the Data and Resources shows such narrower confidence intervals and how they can even be further reduced with additional years of simulation.

Prior distribution

To define the prior, we estimated the mean recurrence of large ruptures in the subduction faults from the Nazca Ridge with latitude −16° (southern boundary of study region) up to Arauco in Chile with latitude −37° (Saillard et al., 2017). The Nazca Ridge has low ISC, and there is no historical rupture that propagated from one region to another; thus we considered that earthquakes in these two regions are independent. We estimated average interseismic times of earthquakes with magnitude above 7.5 for fault cross-sections each 1°. We used the resulting median of ∼165 years from these estimates as the prior median.

For α_j, prior medians were set to 0.7, a value that has been used extensively in BPT distributions and earthquake hazard models (Field et al., 2015). For γ, the prior median was set to 375 km, which equals the calibrated values found in previous analyses of the seismic region (Ceferino et al., 2018).

Because this is a sparse-data problem, we use a weakly informative priors instead of an uninformative prior. We tested two logarithmic standard deviations (LSD's) for all fault parameters of 0.8 and 1.2. These LSD's capture high uncertainties in the apriori knowledge of the fault and were set with the purpose of statistical regularization. We estimated an LSD of 0.8 in the average interseismic times in the fault cross-sections from the Nazca Ridge to Arauco, indicating considerable uncertainty in the large-earthquake recurrence in these neighboring faults, which is consistent with the LSD values in the prior.

Preprocessing synthetic catalogs

First, we removed aftershocks. Similarly to the procedure by Felzer et al. (2004), we identified aftershocks as events that occurred within 2.5 times the mainshock's rupture length from mainshock's epicenter. We also consider that aftershocks could happen up to 30 days after the mainshock and that their magnitude had to be at least 1.2 smaller than the mainshock magnitude (Shcherbakov et al., 2013). Additionally, we observed earthquake doublets in the synthetic catalogs, pairs of subsequent events occurring within temporal windows that span from weeks to a couple of years and occurring close to each other. Because the probabilistic model captures long-term earthquake recurrence rather than short-term recurrence, we lumped doublets into one more massive complex earthquake with equivalent aggregated magnitude (see a similar approach in Ceferino et al. (2020)).

First update with synthetic data

We ran the first Bayesian update using MCMC. Descriptions about the convergence of the likelihood function in the Bayesian update can be found in Ceferino et al. (2018). We obtained 10,000 samples of the parameters and calibrated the random walk to achieve between 20-26% acceptance rate. This rate falls within the desired range for good "mixing", i.e., effective exploration of the high-probability regions in the high-dimensional parameter space (Chib and Greenberg, 1995; Robert, 2014). We deemed that the first 900 samples were part of the burn-in period because they still belonged to the parameter space's low-probability regions.

We conducted updates on 18 cases to account for priors with two different LSD's and nine synthetic catalogs. Figure 8 shows the marginal posteriors of μ_4 for the 18 cases. While we only show a marginal distribution, the update is conducted over the joint distribution of 17 parameters. The plots with posteriors of all other parameters are included in Supplementary Figures 8 and 10.

Because the synthetic catalogs exhibit a broad variety of earthquake cycles (Figure 5), they generate different posterior distributions. Specifically, the posteriors resulted in distributions with markedly different medians. In contrast to the synthetic catalogs' large effect on the medians, the prior selection had little effect on them (Figures 8a and 8b). For μ_4, synthetic catalogs A-2 and A-3 give posterior medians in the range between 80 and 110 years, whereas synthetic catalogs A-1 and C-3 between 110 and 140 years. Synthetic catalogs B-1 and B-2 give medians between 160 and 210 years, whereas synthetic catalogs B-3 and C-2 between 220 and 260 years. Synthetic catalog C-1 shows a median of ∼380 years. These different estimates in μ_4's posterior median can be partially explained by the seemingly different rupture recurrences in the synthetic catalogs in section 4, with longer interseismic times for case C (Figure 5). However, all parameters are updated jointly; thus, μ_4's median estimates incorporate information of interactions between all sections' recurrences.

The adopted LSD's of 0.8 and 1.2 in the weakly informative prior regularize the posterior distribution at different levels, where the latter case leads to generally larger LSD's in the posterior (wider posteriors in Figure 8a than in 8b). We observed expected high reductions in the SD's of the parameter distributions through the inclusion of synthetic catalogs. When the priors with LSD of 0.8 and 1.2 are updated with catalog B-2 (before the synthetic catalogs' uncertainty is propagated), the μ_4's posteriors have SD's 87% and 96% lower than in their respective priors. With catalog B-2, the average SD reductions for all parameters are 88% and 96%, respectively. Generally, larger relative reductions in SD are found for the priors with larger LSD (Supplementary Tables 2 and 3 and Supplementary Figures 7 and 9).

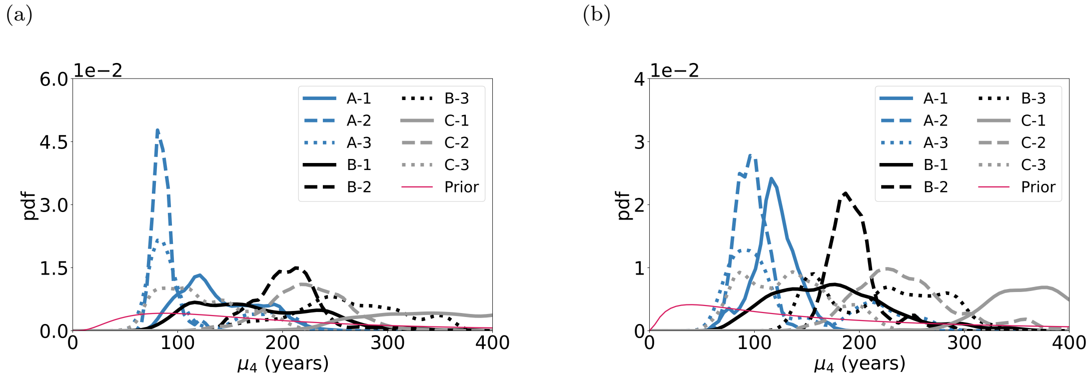

Figure 8: Marginal posterior distributions of μ_4 after update with nine different synthetic catalogs. (a) A prior distribution of median of 165 years and LSD of 0.8 is used. b) A prior distribution of median of 165 years and LSD of 1.2 is used. A Gaussian kernel was used to depict the pdf's as continuous curves.

Second update with historical data

In the second update, we incorporated the historical catalog using the same procedure for the first update. To leverage the same algorithm described previously, we used MLE to fit independent lognormal distributions to the 18 posteriors' samples from the first update. Other fitting techniques, such as the method of moments, can also be used. The fitted curves were used as priors for the second update.

Like the first update, the second update is conducted over the joint distribution of the 17 parameters. Figure 9 shows the marginal posteriors for μ_4, and Supplementary Figures 10 and 11 and Supplementary Tables 4-21 summarize the posteriors for all other parameters. The second update refines the posterior medians with the historical catalog, with stronger μ_4 median variations for synthetic catalogs B-1, B-2, C-1, and C-3 (from 170 to 210, 200 to 170, 370 to 290, and 120 to 170 years, respectively). The contrast between Figures 9 and 8 shows that the variability between posteriors decreases after the second step, mainly driven by the reduction in interseismic times for posteriors with high values in the first update, e.g., catalog C-1 in Figure 8. This variability reduction is due to the use of a unique historical catalog for all posteriors from the first update. Additionally, we observed further reductions in SD after performing the second update, i.e., each posterior becomes less wide. For example, for the synthetic catalog B-2, the total reduction in the μ_4's SD is 90% from the initial prior with LSD of 0.8, 3% more than the decrease in the first update. For all parameters, the average reduction is 91%, a 3% additional decrease to the first update. We found additional SD decreases of 1% for both μ_4 and the average case, respectively, for the initial prior with LSD of 1.2. Note that these reductions are still important because the initial priors had significantly larger SD's relative to the ones in the posteriors.

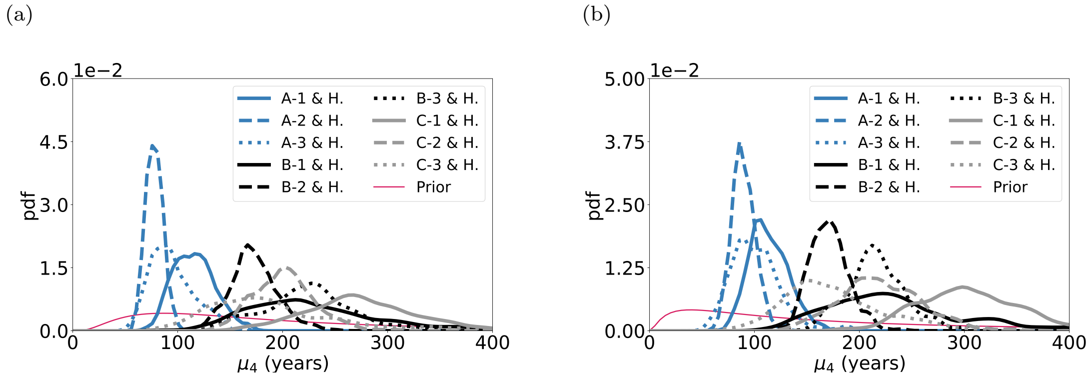

Figure 9: Marginal posterior distributions of μ_4 after the first and second Bayesian updates. (a) A prior distribution with median of 165 years and LSD of 0.8 is used. b) A prior distribution with median of 165 years and LSD of 1.2 is used. A Gaussian kernel was used to depict the pdf's as continuous curves.

Combining multiple synthetic catalogs and propagating their uncertainty

To account for the variability between synthetic catalogs, we combined all two-step posteriors following Equation 22. We estimated $f(\epsilon_{\mathrm{ISC}})$ and $f(\Delta\tau)$ to determine each catalogs' likelihood. For each catalog, we estimated ϵ_{ISC} as the RMS of the difference between its ISC and the mean GPS-inferred ISC in Figure 6. Each catalog's ISC was computed after a synthetic earthquake cycle similar to the one preceding the GPS data collection from 2008 to 2013 (Supplementary Figure 3). Through ISC, $f(\epsilon_{\mathrm{ISC}})$ accounts for spatial matching to the fault seimotectonics. $f(\epsilon_{\mathrm{ISC}})$ is a normal distribution with mean of 0 (maximum at ϵ_{ISC} of 0) and SD of 0.1, found from the average standard deviation between the five GPS-inferred ISC estimates by Villegas-Lanza et al. (2016) (Supplementary Figure 12a). $f(\Delta\tau)$ is a lognormal distribution with a median of 1.6 MPa and LSD of 0.91, found from the empirical global distribution for reverse earthquakes with magnitude larger than 7.5 in Allmann and Shearer (2009) (Supplementary Figure 12b). For each catalog, $\Delta\tau$ was estimated as the median stress drop across their large-magnitude earthquakes. As described previously, synthetic catalogs had different $\Delta\tau$ according to the physics-based input data, leading to different interseismic times in the simulations (Figure 5). Thus, through $\Delta\tau$, $f(\Delta\tau)$ accounts for temporal matching to the fault's seismotectonics.

Figure 10 shows the resulting marginal distribution for μ_4, and Supplementary Figures 13 and 14 and Supplementary Tables 22 and 24 include plots and tables summarizing the results for all other parameters. For comparison, we ran a one-step Bayesian update using only the historical catalog for both initial priors, with LSD's of 0.8 and 1.2. For the prior with LSD of 0.8, the posterior median of μ_4 results in 143 years when all nine two-step posteriors are combined, whereas this median is 103 years when only the historical catalog is used. This difference is a significant 39% increase in μ_4 when synthetic catalogs are included. However, on average for all parameters, medians for μ_j are only 11% higher for this case. We obtained similar results for the prior with LSD of 1.2, further demonstrating that this application's prior selection had an insignificant effect on the posterior medians.

Our analysis also shows whether the use of synthetic catalogs can alleviate large parameter uncertainties by lowering their posteriors' SD's. For μ_4, the SD is 65% and 89% smaller than the initial weakly informative priors with LSD of 0.8 and 1.2, respectively (Supplementary Figures 23 and 25). These reductions are smaller than in the individual two-step posteriors reported previously because the combination of catalogs propagates the additional uncertainty contained in the physics-based simulation. For example, the two-step posterior with the synthetic catalog B-2 resulted in larger SD reductions of 90% and 96% for the prior with LSD's of 0.8 and 1.2, respectively. Figure 11 demonstrates that this

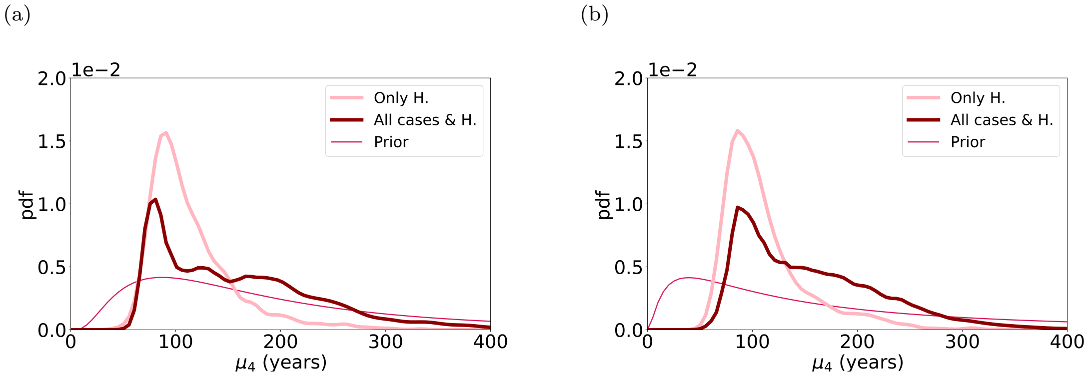

Figure 10: Marginal distribution of μ_4 for prior, a one-step posterior with the historical catalog, and the combination of all the two-step posteriors. A Gaussian kernel was used to depict the pdf's as continuous curves. (a) The initial prior had an LSD of 0.8. (b) The initial prior had an LSD of 1.6.

observation holds for most parameters.

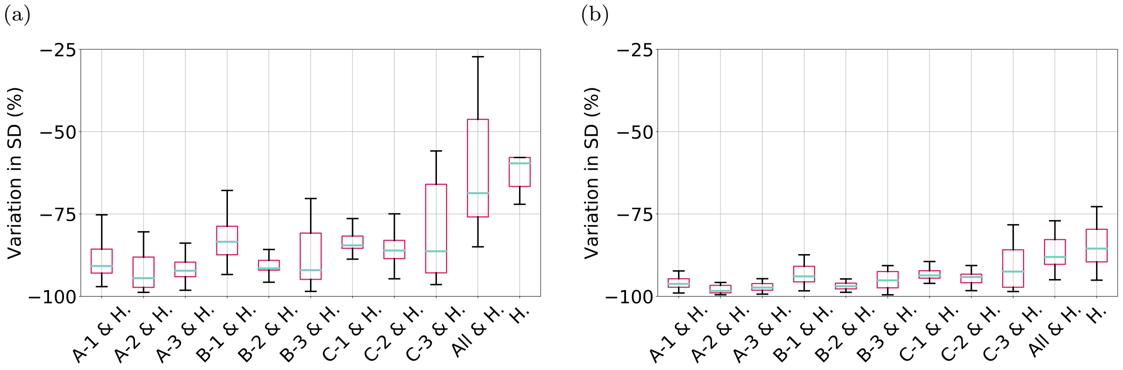

Figure 11: Box plots showing variations in SD for all parameters relative to the initial prior distribution after nine different two-step updates, the combination of all two-step posteriors, and a one-step update with only the historical catalog. The variations in SD are estimated for the 17 parameter, and the boxes highlight their median, lower quartile and upper quartile. a) Initial prior distribution with LSD of 0.8. b) Initial prior distribution with LSD of 1.2.

The plot also shows SD's reductions when only the historical catalog is used. Figure 11a shows that when the prior has an LSD of 0.8, the median parameter has higher uncertainty reductions (-69% vs. -60%) through the incorporation of synthetic catalogs. However, the highest uncertainty parameters perform better without the synthetic catalogs as indicated by the upper quartiles (-46% vs. -58%). When the initial prior is more uncertain, represented through the LSD of 1.2, Figure 11b demonstrates that synthetic catalogs reduce uncertainty in the parameter estimates more effectively than for the less uncertain prior. Medians and even upper quartiles in the box plots show higher reductions in SD's by including the synthetic catalogs (-88% vs. -86%, and -83% vs. -80%, respectively), indicating better performance than only using the historical catalog.

Because the historical catalog is sparse, we observe that synthetic catalogs can effectively decrease high uncertainties in priors. These results imply that while synthetic catalogs' uncertainty is high, they can supplement short historical catalogs to determine interseismic times under a Bayesian framework, especially for tectonic regions with a marked lack of apriori knowledge about the recurrence of large earthquakes.

SEISMIC HAZARD

To assess synthetic catalogs' effect on time-dependent seismic hazard, we estimate the likelihood of exceeding peak ground accelerations (PGA) of 0.1 g in the next 30 years due to earthquakes with magnitudes larger than 7.5 and utilized a similar procedure as Ceferino et al. (2020). We used parameter values equal to the medians of the posterior distribution for two cases updating the initial prior with LSD of 0.8: the one-step posterior using only the historical catalog, and the combination of all nine two-step posteriors for different synthetic catalogs. Seismic hazard for the former case is higher in the central region (Figures 12a) because, unlike the regions close to the boundaries, it has contributions from large earthquakes rupturing both southern and northern neighboring regions (see similar observations in Ceferino et al. (2020)).

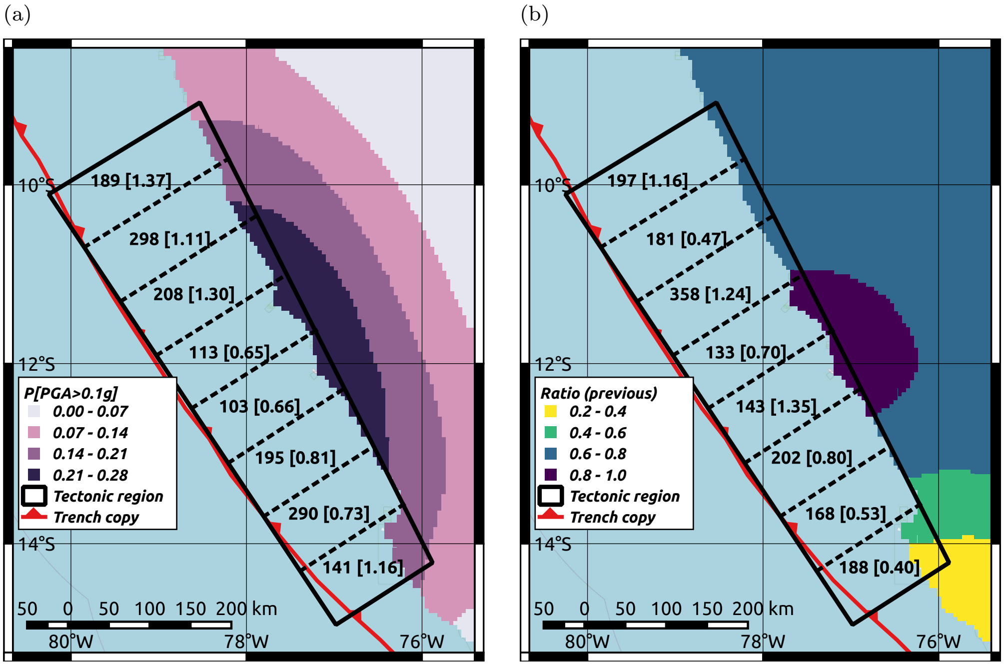

Figure 12: Time-dependent seismic hazard in terms of probability of PGA exceeding 0.1 g in the next 30 years using the rupture model fitted using different cases. (a) One-step update with only historical data. (b) Combination of two-step update using nine synthetic catalogs with the historical data represented as a fraction of the hazard estimates in (a). Mean interseimic times and coefficient of variations (μ_j in years, $[\alpha_j]$) used to evaluate hazard are indicated within each fault section.

Combining the synthetic data with the historical data results in hazard estimates that are 60-100% of the historical-only case in most regions (Figure 12b). Previously, we noted that variations in median interseismic times (μ_j values used to estimate the hazard) were only of 11%, on average, across the fault sections. In contrast, seismic hazard exhibits more considerable variations when synthetic data are incorporated. Such dissimilarities arise from the μ_j and marginal hazard rate variations in individual sections. For the six northern sections, μ_j is higher in five of them when the synthetic catalog is incorporated, notably by 39% and 72% in sections 4 and 6, respectively. Higher μ_j values lead to longer earthquake recurrences and, thus, lower seismic hazard. While we find that section 7 has 39% lower μ_7 when the synthetic catalogs are added, its hazard rate is still lower because of its lower α_7 value. In BPT distributions, lower α_7 values indicate more periodic ruptures, with lower probabilities of ruptures occurring with times significantly different from μ_j. In section 7, the seismic gap is $\sim$50 years; thus, such a low gap compared to μ_7 (181 years) results in a lower hazard when the synthetic catalogs are included, even though its μ_7 value is shorter than 298 years (Supplementary Figure 15). Turning to the southern region, we observe that incorporating synthetic data lowers the hazard more significantly (to 20-40%). The time-dependent seismic hazard is particularly sensitive to variations in μ_j in this region because the likelihood of earthquake occurrence is inherently low due to the recent 2007 Pisco earthquake. The 33% longer μ_1 after including the synthetic data largely contributes to its lower hazard estimates. Additionally, similar to section 7, lower values α_1 and α_2 further contribute to the low probability of large rupture for the next 30 years in sections 1 and 2 when the synthetic catalogs are included (Supplementary Figure 15).

SUMMARY AND CONCLUSIONS

This paper presents a framework to supplement short historical catalogs with synthetic catalogs and determine large earthquakes' recurrence. The framework is based on a parameter estimation technique for a probabilistic time- and space-interaction model of mainshock earthquake occurrence. The proposed parameter estimation conducts a first Bayesian update utilizing a physics-based synthetic catalog followed by a second Bayesian update using the historical catalog. For the Bayesian update, we presented a formulation to evaluate both the prior distribution and the likelihood of observing earthquake data under the probabilistic mainshock earthquake occurrence model. We also formulated an MH MCMC procedure to find the posterior distribution of the parameters. To account for the uncertainty in physics-based models, we also presented a formulation to combine the posteriors resulting from updates with different synthetic catalogs using the catalogs' likelihood of representing the fault's ISC and empirical stress drops.

This paper applied the proposed parameter estimation technique to study earthquakes with magnitudes larger than 7.5 in the subduction zone offshore of Lima, Peru. We utilized a 450-year-long historical catalog, and additionally, we built nine 2,000-year-long synthetic catalogs for the region utilizing physics-based simulation and high-performance computing. We accounted for uncertainty in the physics-based model by varying critical input data and asperity regions' properties based on past earthquakes. We validated the synthetic catalogs by verifying that they can reproduce feasible earthquake cycles and annual magnitude exceedance rates compared to existing historical catalogs.

We applied the proposed two-step Bayesian update to estimate the posterior distribution of the probabilistic model's parameters using two weakly informative priors with LSD's of 0.8 and 1.2. The second prior had a 50% longer LSD representing a deeper state of lack of knowledge about large-earthquake recurrence in the fault. After conducting two-step updates using the historical catalog and the nine synthetic catalogs, we showed that synthetic catalogs effectively supplement the short historical catalog with significant decreases in the posterior uncertainty. For example, with synthetic catalog B2, we found average reductions of 91% and 97% for the priors with LSD's of 0.8 and 1.2, respectively. While medians in the posterior were only a little sensitive to prior selection, the relative decreases in uncertainty were higher for the prior with larger LSD, i.e., higher state of lack of apriori knowledge. However, our results also demonstrated that the parameter posterior distribution parameter is sensitive to synthetic catalog selection due to the wide variety of feasible conditions represented in the physics-based simulation.

We combined the nine different two-step updates using our proposed formulation to account for the uncertainty in the physics-based simulation uncertainty. We compared the results to a baseline that only uses the historical catalog to update the two weakly informative priors. We showed that supplementing the short historical catalog with synthetic catalogs reduces uncertainty for the median parameter (69%) to a higher degree than the baseline (60%) for the prior with LSD of 0.8. When less is known about the fault, represented through the prior with 1.2 LSD, synthetic catalogs proved to be even more valuable. They successfully reduced uncertainty even for parameters with larger standard deviations (83%) than the baseline (80%). Our results advocate for extending the usage of synthetic catalogs, especially in regions where prior knowledge about the fault is little, as demonstrated in our case study in Peru.

Finally, we evaluated the time-dependent hazard. We calculated the probability of exceeding a PGA of 0.1g during the next 30 years using the medians of the parameters from both the combination of the nine two-step posteriors and the one-step posterior using only the historical catalog. We showed that the synthetic catalogs' inclusion results in 20%-40% smaller hazard estimates in most of the fault. The lower hazard estimates are mainly explained by the longer interseismic times found from including the synthetic catalogs (11% higher on average). In the southern region, we found notably lower hazard estimates (60%-80% lower) after including synthetic catalogs mainly because time-dependent hazard is particularly sensitive to regions with recent ruptures. With these results, we show that hazard estimates are not proportional to the variations in interseismic times stemming from including synthetic catalogs, especially for regions with recent ruptures.

DATA AND RESOURCES

The code to reproduce the two-step parameter estimation, one-step parameter estimation, and hazard assessment can be found at `https://purl.stanford.edu/mf336sw2626` (last accessed June 2020). The QDYN open-source software needs to be installed to generate the synthetic data and is available at `https://github.com/ydluo/qdyn` (last accessed June 2020). The data including the nine synthetic rupture simulations is available at `https://purl.stanford.edu/by735ng7322` (last accessed June 2020).

Acknowledgments

We thank the Stanford Research Computing Center for providing computational resources. We acknowledge Dr. Heresi from Stanford University for insightful discussions on the uncertainty of historical catalogs. We acknowledge the support by the Shah Family Fellowship, the Jhon A. Blume Fellowship from the Civil Engineering Department at Stanford University, and the Postdoctoral Fellowship from the Andlinger Center at Princeton University. We acknowledge the support by the French government through the UCAJEDI Investments in the Future project managed by the National Research Agency (ANR) with the reference number ANR-15-IDEX-01. The authors also appreciate the constructive comments and suggestions of the BSSA reviewers of the paper.

References

Akinci, A., Galadini, F., Pantosti, D., Petersen, M., Malagnini, L., and Perkins, D. (2009). Effect of time dependence on probabilistic seismic-hazard maps and deaggregation for the central Apennines, Italy. *Bulletin of the Seismological Society of America*, 99(2 A):585–610.

Allmann, B. P. and Shearer, P. M. (2009). Global variations of stress drop for moderate to large earthquakes. *Journal of Geophysical Research: Solid Earth*, 114(1):1–22.

Ampuero, J.-P. and Rubin, A. M. (2008). Earthquake nucleation on rate and state faults – Aging and slip laws. *Journal of Geophysical Research*, 113(B01302):1–21.

Barbot, S., Lapusta, N., and Avouac, J.-p. (2012). Under the Hood of the Earthquake Machine: Toward Predictive Modeling of the Seismic Cylce: Supplementary Material. *Science*, 336(May):1–20.

Bradley, A. M. (2014). Software for Efficient Static Dislocation-Traction Calculations in Fault Simulators. *Seismological Research Letters*, 85(6):1358–1365.

Ceferino, L., Kiremidjian, A., and Deierlein, G. (2017). Space and time interaction modeling of earthquake rupture occurrence. In *12th International Conference on Structural Safety and Reliability*, pages 694–703, Vienna, Austria.

Ceferino, L., Kiremidjian, A., and Deierlein, G. (2018). Parameter Estimation Methods for Modeling of Time and Space Interactions of Earthquake Rupture. In *16th European Conference on Earthquake Engineering*, Thessaloniki.

Ceferino, L., Kiremidjian, A., and Deierlein, G. (2020). Probabilistic space- and time-interaction modeling of mainshock earthquake rupture occurrence. *Bulletin of the Seismological Society of America*, Accepted for Publication.

Chhikara, A. R. S. and Folks, J. L. (1977). The Inverse Gaussian Distribution as a Lifetime Model. *Technometrics*, 19(4):461–468.

Chib, S. and Greenberg, E. (1995). Understanding the Metropolis-Hastings Algorithm. *The American Statistician*, 49(4):327–335.

Chlieh, M., Avouac, J. P., Sieh, K., Natawidjaja, D. H., and Galetzka, J. (2008). Heterogeneous coupling of the Sumatran megathrust constrained by geodetic and paleogeodetic measurements. *Journal of Geophysical Research: Solid Earth*, 113(5):1–31.

Day, S., Dalguer, L., Lapusta, N., and Liu, Y. (2005). Comparison of finite difference and boundary integral solutions to three-dimensional spontaneous rupture. *Journal of Geophysical Research*, 110(B12307).

Dieterich, J. H. (1979). Modeling of rock friction: 1. Experimental results and constituve equations. *Journal of geophysical research*, 84(9):2161–2168.

Dieterich, J. H. and Kilgore, B. D. (1994). Direct observation of frictional contacts: New insights for state-dependent properties. *Pure and Applied Geophysics*, 143(1-3):283–302.

Felzer, K. R., Abercrombie, R. E., and Ekström, G. (2004). A common origin for aftershocks, foreshocks, and multiplets. *Bulletin of the Seismological Society of America*, 94(1):88–98.

Field, E. H. (2015). Computing Elastic-Rebound-Motivated Earthquake Probabilities in Unsegmented Fault Models: A New Methodology Supported by Physics-Based Simulators. *Bulletin of the Seismological Society of America*, 105(2A):544–559.

Field, E. H., Biasi, G. P., Bird, P., Dawson, T. E., Felzer, K. R., Jackson, D. D., Johnson, K. M., Jordan, T. H., Madden, C., Michael, A. J., Milner, K. R., Page, M. T., Parsons, T., Powers, P. M., Shaw, B. E., Thatcher, W. R., Weldon, R. J., and Zeng, Y. (2015). Long-Term Time-Dependent Probabilities for the Third Uniform California Earthquake Rupture Forecast (UCERF3). *Bulletin of the Seismological Society of America*, 105(2A):511–543.

Galvez, P., Ampuero, J. P., Dalguer, L. A., Somala, S. N., and Nissen-Meyer, T. (2014). Dynamic earthquake rupture modelled with an unstructured 3-D spectral element method applied to the 2011 M9 Tohoku earthquake. *Geophysical Journal International*, 198(2):1222–1240.

Hamra, G., MacLehose, R., and Cole, S. (2013). Sensitivity Analyses for Sparse-Data Problems—Us Weakly Informative Bayesian Priors. *Epidemiology*, 24(2):233–239.

Hayes, G. P., Moore, G. L., Portner, D. E., Hearne, M., Flamme, H., Furtney, M., and Smoczyk, G. M. (2018). Zone Geometry Model. 61(October):58–61.

Ito, T., Yoshioka, S., and Miyazaki, S. (2000). Interplate coupling in northeast Japan deduced from inversion analysis of GPS data. *Earth and Planetary Science Letters*, 176(1):117–130.

Jin, R., Wang, S., Yan, F., and Zhu, J. (2015). Generating Spatial Correlated Binary Data Through a Copulas Method. *Science Research*, 3(4):206–212.

Kaneko, Y., Avouac, J. P., and Lapusta, N. (2010). Towards inferring earthquake patterns from geodetic observations of interseismic coupling. *Nature Geoscience*, 3(5):363–369.

Kendrick, E., Bevis, M., Smalley, R., Brooks, B., Vargas, R. B., Lauría, E., and Fortes, L. P. S. (2003). The Nazca-South America Euler vector and its rate of change. *Journal of South American Earth Sciences*, 16(2):125–131.

Konca, a. O., Fang, P., Li, Z., Galetzka, J., Genrich, J., and Chlieh, M. (2007). Partial rupture of a locked patch of the Sumatra megathrust during the 2007 earthquake sequence. *Nature*, pages 1–24.

Lapusta, N. and Liu, Y. (2009). Three-dimensional boundary integral modeling of spontaneous earthquake sequences and aseismic slip. *Journal of Geophysical Research: Solid Earth*, 114(9):1–25.

Liu, J. S. (2004). *Monte Carlo Strategies in Scientific Computing*. Springer Series in Statistics. Springer New York, New York, NY.

Liu, Y. and Rice, J. R. (2007). Spontaneous and triggered aseismic deformation transients in a subduction fault model. *Journal of Geophysical Research: Solid Earth*, 112(9):1–23.

Lohman, R. B. and McGuire, J. J. (2007). Earthquake swarms driven by aseismic creep in the Salton Trough, California. *Journal of Geophysical Research: Solid Earth*, 112(4):1–10.

Luo, Y., Ampuero, J. P., Galvez, P., van den Ende, M., and Idini, B. (2017). QDYN: a Quasi-DYNamic earthquake simulator (v1.1).

Marone, C. (1998). Laboratory-Derived Friction Laws and Their Application To Seismic Faulting. *Annual Review of Earth and Planetary Sciences*, 26(1):643–696.

Marone, C. and Kilgoret, B. (1993). (1993) Scaling of the critical slip distance for seismic faulting with shear strain in fault zones [Marone & Kilgore 1993 Nature].pdf. 362(April):618–621.

Papazachos, B., Scordilis, E., Panagiotopoulos, D., Papazachos, C., and Karakaisis, G. (2004). Global Relations between Seismic Fault Parameters and Moment Magnitude of Earthquakes. *Bulletin of the Geological Society of Greece*, 36(3):1482–1489.

Parsons, T., Console, R., Falcone, G., Murru, M., and Yamashina, K. (2012). Comparison of characteristic and Gutenberg-Richter models for time-dependent M 7.9 earthquake probability in the Nankai-Tokai subduction zone, Japan. *Geophysical Journal International*, 190(3):1673–1688.

Richards-Dinger, K. and Dieterich, J. H. (2012). RSQSim Earthquake Simulator. *Seismological Research Letters*, 83(6):983–990.

Robert, C. P. (2014). The Metropolis-Hastings algorithm. *Wiley StatsRef: Statistics Reference Online*, pages 1–15.

Rubin, A. M. and Ampuero, J. P. (2005). Earthquake nucleation on (aging) rate and state faults. *Journal of Geophysical Research: Solid Earth*, 110(11):1–24.

Ruina, A. (1983). Slip instability and state variable friction laws. *Journal of Geophysical Research: Solid Earth*, 88(B12):10359–10370.

Saillard, M., Audin, L., Rousset, B., Avouac, J. P., Chlieh, M., Hall, S. R., Husson, L., and Farber, D. L. (2017). From the seismic cycle to long-term deformation: linking seismic coupling and Quaternary coastal geomorphology along the Andean megathrust. *Tectonics*, 36(2):241–256.

Savage, J. C. and Langbein, J. (2008). Postearthquake relaxation after the 2004 M6 Parkfield, California, earthquake and rate-and-state friction. *Journal of Geophysical Research: Solid Earth*, 113(10):1–17.

Seiner, L. (2011). *Historia de los sismos en el Perú. Catálogo: Siglos XVIII-XIX.* Universidad de Lima. Fondo Editorial, Lima, Peru.

Shcherbakov, R., Goda, K., Ivanian, A., and Atkinson, G. M. (2013). Aftershock statistics of major subduction earthquakes. *Bulletin of the Seismological Society of America*, 103(6):3222–3234.

Silgado, E. (1978). Historia de los Sismos más Notables Ocurridos en el Perú (1513-1974). In Instituto de Geología y Minería, editor, *Serie C. Geodinámica e Ingeniería Geológica. Boletín No. 3*, Lima, Peru.

Sykes, L. R. and Menke, W. (2006). Repeat times of large earthquakes: Implications for earthquake mechanics and long-term prediction. *Bulletin of the Seismological Society of America*, 96(5):1569–1596.

Tullis, T. E. (1988). *Rock friction constitutive behavior from laboratory experiments and its implications for an earthquake prediction field monitoring program*, volume 126.

Tweedie, M. C. K. (1957). Statistical Properties of Inverse Gaussian Distribution I. *The Annals of Mathematical Statistics*, 28(2):362–377.

Ulm, K. (1990). Simple method to calculate the confidence interval of a standardized mortality ratio (SMR). *American Journal of Epidemiology*, 131(2):373–375.

Villegas-Lanza, J. C., Chlieh, M., Cavalié, O., Tavera, H., Baby, P., Chire-Chira, J., and Nocquet, J.-M. (2016). Active tectonics of Peru: Heterogeneous interseismic coupling along the Nazca megathrust, rigid motion of the Peruvian Sliver, and Subandean shortening accomodation. *Journal of Geophysical Research : Solid Earth*, pages 1–24.

Wells, D. L. and Coppersmith, K. J. (1994). New Empirical Relationships among Magnitude, Rupture Length, Rupture Width, Rupture Area, and Surface Displacement. *Bulletin of the Seismological Society of America*, 84(4):974–1002.